Interaction of a surface wave with a dislocation

Agnès Maurel,[1] Vincent Pagneux,[2] Felipe Barra,[3,4] and Fernando Lund[3,4]
[1]*Laboratoire Ondes et Acoustique, UMR CNRS 7587, Ecole Supérieure de Physique et de Chimie Industrielles, 10 rue Vauquelin, 75005 Paris, France*
[2]*Laboratoire d'Acoustique de l'Université du Maine, UMR CNRS 6613, Avenue Olivier Messiaen, 72085 Le Mans Cedex 9, France*
[3]*Departamento de Física, Facultad de Ciencias Físicas y Matemáticas, Universidad de Chile, Casilla 487-3, Santiago, Chile*
[4]*Centro para la Investigación Interdisciplinaria Avanzada en Ciencias de los Materiales (CIMAT), Universidad de Chile, Santiago, Chile*
(Received 13 December 2006; published 18 June 2007)

The scattering of a surface wave by a pinned edge dislocation in a semi-infinite, homogeneous, isotropic, three-dimensional elastic solid is investigated analytically and numerically. An incident wave excites the dislocation that responds by oscillating as a string endowed with mass, line tension, and damping. The oscillations of the stringlike dislocation generate secondary ("scattered") elastic waves that are the primary object of interest in this study. The back reaction of the re-emitted waves on the dislocation dynamics is neglected, but the wavelength of the radiation is allowed to be large, comparable, or small compared to the length of the dislocation. In view of recent experimental visualizations of these phenomena, we focus particularly on the field behavior at the free surface near the dislocation, and not just on the far field. For the same reason, it is the vertical component of displacement at the free surface that is studied in detail. An efficient numerical procedure for the computation of the appropriate components of the Green's function, using a Filon quadrature for the integration of rapidly oscillating functions, is developed. The numerics is validated with known analytical expressions. The secondary radiation generated by the response of the dislocation to the incident wave is also calculated numerically, and the results are also validated by comparing them with the analytical expressions that can be obtained when the radiation wavelength is very long compared to dislocation length. The interference pattern between incident wave and secondary wave that is generated at the free surface is studied in detail and found to depend strongly not only on wavelength and dislocation geometry (length and orientation) but also on dislocation depth, with the response of the dislocation being a particularly sensitive function of such depth. Results are compared with recent experiments of Shilo and Zolotoyabko [Phys. Rev. Lett. **91**, 115506 (2003)] that report visualizations of the surface-wave–dislocation interaction using stroboscopic x-ray imaging. A satisfactory agreement is found. Dislocation velocities of a few percent of the speed of sound and viscosity coefficients of about 10^{-5} Pa s are inferred.

DOI: 10.1103/PhysRevB.75.224112 PACS number(s): 61.72.Lk, 72.10.Fk, 11.80.La, 81.70.Cv

I. INTRODUCTION

Dislocations lie at the heart of the mechanical behavior of crystalline materials, and yet they are extremely difficult to probe. Transmission electron microscopy has long been the tool of choice for their experimental study, and impressive results, for example, concerning core structure, have recently been obtained in conjunction with progress in instrumentation and computational capabilities (see, for example, Ref. 1 and references therein). The fact remains, however, that transmission electron microscopy needs the special preparation of samples and that the development of nonintrusive probes, for example, involving acoustic or electromagnetic waves, would be a welcome development.

The interaction of phonons with dislocations is a problem that has been studied for decades in connection with acoustic attenuation and thermal conductivity. For a long time, acoustics results appeared to be satisfactorily explained by quantitative modeling developed in the 1950s and subsequent elaborations.[2] That modeling, based on a scalar coherent wave propagating through a medium with many dislocations, has become unable to explain recent experiments, such as the different attenuations observed for acoustic and shear waves.[3] Being an effective medium approximation, it only describes the coherent behavior of a wave propagating in a medium full of dislocations and is unable to describe the interaction of an incident wave with a single dislocation. The situation concerning thermal conductivity is even less satisfactory, with results going back 20 years[4] that still defy quantitative understanding.

In light of the above, we decided to revisit the basic physics of the wave-dislocation interaction[5–10] succeeding, for example, in explaining the results of Ref. 3.

Recently, Zolotoyabko *et al.*[11] Shilo and Zolotoyabko[12,13] have conducted a series of experiments where they study the interaction of surface elastic waves with dislocations in $LiNbO_3$ using stroboscopic x-ray topography. They have shown that the effect of a single dislocation on the surface acoustic wave is strong enough to produce a scattered wave that forms, with the incident wave, an observable interference pattern. Also, Hurley *et al.*[14] have also performed a similar study, using an optical technique, of the interference patterns in the case of the interaction of an elastic wave with grain boundaries. These experiments illustrate the potential that acoustic diagnostics has as a nonintrusive tool to characterize defects in materials, and they offer an experimental benchmark that can be used to examine the theoretical models for the interaction of isolated dislocations with elastic waves.

The present paper studies the problem of the interaction of a surface Rayleigh wave propagating in a semi-infinite

elastic medium, with subsurface dislocation lines. Following our previous work[5–10] that studied the interaction of bulk acoustic waves with dislocations, we examine the experimental configuration presented in Ref. 13 and illustrated in Fig. 5: a Rayleigh wave propagates on the surface of an elastic material containing in its bulk an edge dislocation line. To do that, the Green's tensor of the half space with free surface has to be numerically calculated, a task known to be tedious. Although many studies can be found on this problem (see, for instance, Refs. 15–21 and references therein), a part of this paper is devoted to its implementation for fast calculations suited to the configuration at hand.

The paper is organized as follows. Section II presents the results on the Green's function for the half space, notably the numerical method (with technical details relegated to the Appendices). These results are validated by comparing them with the analytical results of Achenbach[21] in the far field. In Sec. III A, we present the model used to describe the scattering of a surface acoustic wave by a subsurface dislocation line. In this model, the scattered wave is written in the form of an integral representation that needs the dislocation motion due to the incident wave to be determined. This is done using the equation of motion for a dislocation loaded by an external stress σ, which in the present case is the stress produced by the incident wave. The case of a dislocation small compared to wavelength is calculated analytically in Sec. III B and used to validate the numerical results of Sec. III A. Sections III C and III D present results on the scattered fields, notably in comparison with Ref. 13, and present a discussion on the scattering strength. The paper ends with some concluding remarks.

II. GREEN'S FUNCTION OF THE HALF SPACE

We consider a semi-infinite isotropic homogeneous elastic medium characterized by its Lamé coefficients (λ,μ) and density ρ, occupying a half space with a free surface. Bulk longitudinal and shear waves have speeds of propagation $c_L=\sqrt{(\lambda+2\mu)/\rho}$ and $c_T=\sqrt{\mu/\rho}$, respectively, with their ratio denoted by $\gamma\equiv c_L/c_T$. Waves with angular frequency ω have a time dependence $e^{-i\omega t}$ and propagate in the bulk with wave vectors $k_{L,T}\equiv\omega/c_{L,T}$. Surface Rayleigh waves propagate with wave vector $k_R\equiv\omega/(\zeta c_T)$, with ζ the zero of $P(\zeta)=\zeta^6-8\zeta^4+8\zeta^2(3-2/\gamma^2)-16(1-1/\gamma^2)$ (see, e.g., Ref. 22). The corresponding wavelength will be denoted as $\lambda_R=2\pi/k_R$.

The literature on the Green's tensor of the half space with free surface is vast, and various derivations of the elastic displacement due to a subsurface point force or other excitation sources can be found.[15–21] We give in this section the result for the vertical displacement that is of interest in our study. Indeed, experiments of surface acoustic wave detection are sensitive to the vertical displacement only. In this case, an easy way to derive it, as written in Eq. (2.1) below, is presented in Appendix A. The main goal of this section is the numerical implementation of the Eq. (2.1) using a Filon-quadrature-type method.

A. Vertical displacement due to a subsurface point force

As shown in Appendix A, the vertical displacement in the frequency domain $u_z(\mathbf{x})$, with $\mathbf{x}=(r\cos\varphi, r\sin\varphi, 0\leqslant z\leqslant z_0)$,

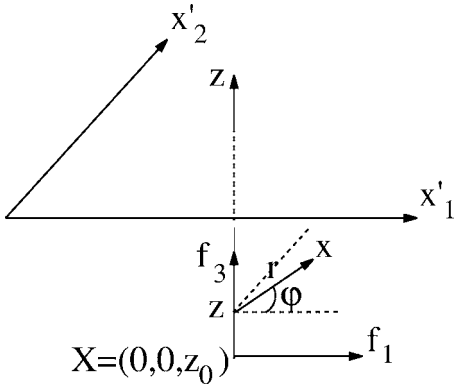

FIG. 1. A subsurface point force $\mathbf{f}=(f_1,0,f_3)\delta(\mathbf{x}-\mathbf{X})$ at $\mathbf{X}=(0,0,z_0)$ creates a displacement $u_z(\mathbf{x})$ at $\mathbf{x}=(r\cos\varphi, r\sin\varphi, z)$ position. Equation (2.1) gives the vertical displacement at $\mathbf{x}$ for $0\geqslant z\geqslant z_0$.

due to a subsurface point force $\mathbf{f}=(f_1,0,f_3)\delta(\mathbf{x}-\mathbf{X})$, with $\mathbf{X}=(0,0,z_0)$ (see Fig. 1), is

$$u_z(\mathbf{x})=\frac{1}{2\pi\mu}\left[(\cos\varphi)f_1\int_0^\infty dkk^2J_1(kr)f(k;z,z_0)+f_3\int_0^\infty dkk\xi_LJ_0(kr)g(k;z,z_0)\right], \tag{2.1}$$

where $\xi_{L,T}\equiv\sqrt{k^2-k_{L,T}^2}$ and where

$$\begin{aligned}2k_T^2f(k;z,z_0)\equiv&[G(k)e^{\xi_Lz_0}+4\xi_L\xi_T(k_T^2-2k^2)e^{\xi_Tz_0}]\frac{e^{\xi_Lz}}{F(k)}\\&+[4k^2(k_T^2-2k^2)e^{\xi_Lz_0}+G(k)e^{\xi_Tz_0}]\frac{e^{\xi_Tz}}{F(k)}\\&+e^{-\xi_L(z-z_0)}-e^{-\xi_T(z-z_0)},\end{aligned} \tag{2.2}$$

$$\begin{aligned}2k_T^2g(k;z,z_0)\equiv&[G(k)e^{\xi_Lz_0}+4k^2(k_T^2-2k^2)e^{\xi_Tz_0}]\frac{e^{\xi_Lz}}{F(k)}\\&+\left[4k^2(k_T^2-2k^2)e^{\xi_Lz_0}+\frac{k^2}{\xi_L\xi_T}G(k)e^{\xi_Tz_0}\right]\frac{e^{\xi_Tz}}{F(k)}\\&+e^{-\xi_L(z-z_0)}-\frac{k^2}{\xi_L\xi_T}e^{-\xi_T(z-z_0)},\end{aligned}$$

with $G(k)\equiv(k_T^2-2k^2)^2+4k^2\xi_L\xi_T$ and $F(k)\equiv(k_T^2-2k^2)^2-4k^2\xi_L\xi_T$. J_n denotes the Bessel function of the first kind of order n. For $f_1=0$, $z=0$, we recover the result given in Ref. 15.

B. Numerical calculation

The expression for the displacement in Eq. (2.1) is known to be difficult to evaluate numerically because of the presence of singularities on the real axis [notably, the Rayleigh pole k_R that makes $F(k)$ to vanish]. A possible way to overcome this difficulty is to consider a viscoelastic case as in Ref. 18, since the singularities then move off the real axis and the numerical integration is possible. There is a second

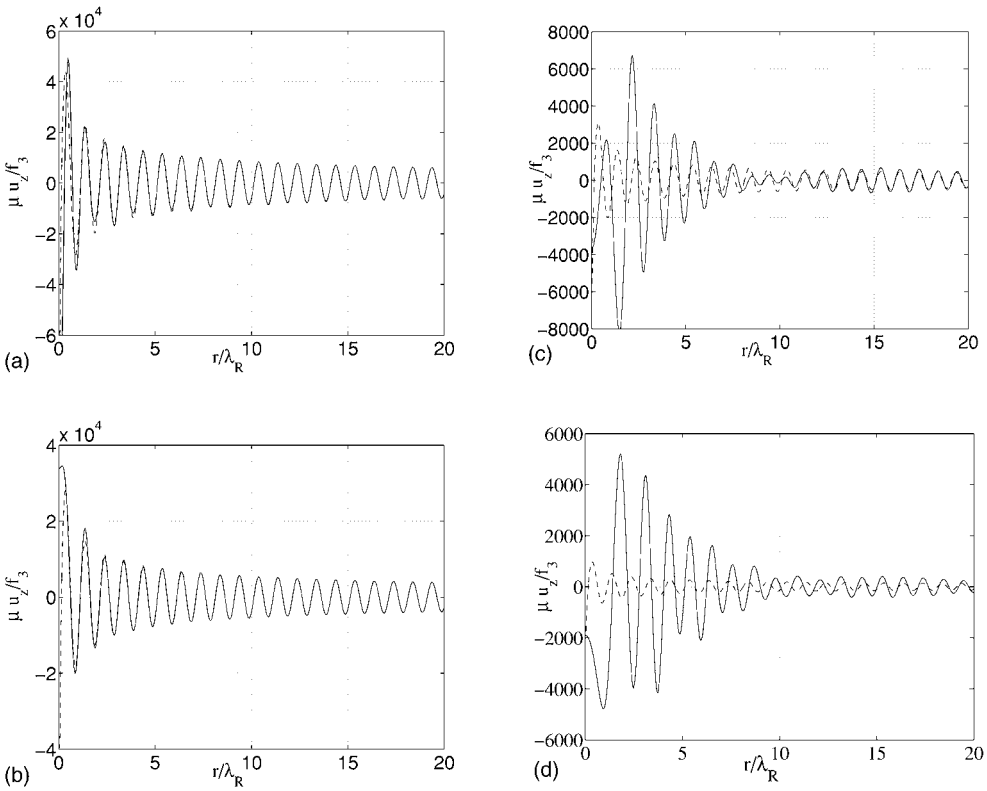

FIG. 2. Comparison of numerical and analytical expressions for the vertical displacement $u_z(\mathbf{x})$ observed at the free surface for a vertical point force f_3 located at depth z_0. Because of axial symmetry, it depends only on the in-plane radial distance r. Full lines give the numerical integration of u_z from Eq. (2.1) calculated with $\epsilon=10^{-10}$, and dashed lines give the analytical solution of Ref. 21 that accounts for the contribution of the Rayleigh pole only. In both cases, calculations are performed using $\omega=(2\pi)(580\times10^6)$ s^{-1}, $c_T=3758$ m/s, $c_L=2c_T$, $\rho=4.6\ 10^3$ kg m^{-3}, and (a) $z_0=-\lambda_R/1000$, (b) $z_0=-\lambda_R/2$, (c) $z_0=-3\lambda_R/2$, and (d) $z_0=-2\lambda_R$.

difficulty that must be overcome for an efficient numerical integration: because of the terms in $J_n(kr)$, the integrands oscillate with a periodicity of $1/r$ that gets smaller and smaller as r increases. This can be tackled using a Filon quadrature[23–25] that makes the integration independent of r, as described in Appendix B.

In light of the above, the results presented in this paper are calculated as follows: the singularities are moved off the real axis by introducing a small imaginary part to the frequency $\omega(1+i\epsilon)$, with ϵ positive in order to ensure causality (with the convention $e^{-i\omega t}$). Practically, $\epsilon=10^{-10}$, a value which appears in the numerics to be small enough to ensure that all the integrals are independent of this particular value of ϵ. The numerical integration on the real axis $[0,\infty]$ is split into a first interval $[0,k_0]$, where a classical Runge-Kutta scheme with adaptative step size is used (typically, we have used $k_0=1.5k_R$), and a second interval $[k_0,k_{max}]$, where a Filon quadrature is used. k_{max} is controlled by the decreasing exponential $e^{\xi_{L,T}z_0}$, and we have used $k_{max}=k_0+10/|z_0|$ (alternatively, when $k_Rz_0\ll1$, we used $k_{max}=50k_R$). The use of the Filon quadratures makes the integration typically ten times faster than a Runge-Kutta method for $k_Rr\sim1$.

Achenbach[21] derived analytically the contribution of the Rayleigh pole that is expected to be the dominant contribution in the in-plane far field. Figure 2 shows the results we have obtained numerically in comparison with the analytical results of Achenbach.[21] As expected, the Rayleigh contribution becomes dominant in the far field, and it is more and more dominant for small r when z_0 is closer and closer to the free surface.

C. Green's tensor

The Green's tensor G^0_{3k} is deduced from the vertical displacement calculated in the previous section through $u_z \equiv G^0_{3j}F_j$, where $\mathbf{F}$ is a subsurface point force expressed in a basis (x_1,x_2,z) that is obtained by a rotation through θ_0 around the vertical axis with respect to the horizontal component of the force f_1, see Fig. 3: $F_1=f_1\cos\theta_0$, $F_2=f_1\sin\theta_0$, and $F_3=f_3$. We thus get $G^0_{31}=u_z|_{(f_1=1,\theta_0=0,f_3=0)}$, $G^0_{32}=u_z|_{(f_1=1,\theta_0=\pi/2,f_3=0)}$, and $G^0_{33}=u_z|_{(f_1=0,f_3=1)}$. Letting $\mathbf{X}=(X_1,X_2,z_0)$, we define the in-plane polar coordinates as $\mathbf{x}=(X_1+r\cos\theta,X_2+r\sin\theta,z)$ (thus, $\varphi=\theta-\theta_0$). With these notations, the Green's tensor relevant for the computation of vertical displacements is

$$G^0_{31}(\mathbf{x},\mathbf{X};\omega)=\frac{1}{2\pi\mu}\cos\theta\int_0^\infty dkk^2J_1(kr)f(k;z,z_0),$$

$$G^0_{32}(\mathbf{x},\mathbf{X};\omega)=\frac{1}{2\pi\mu}\sin\theta\int_0^\infty dkk^2J_1(kr)f(k;z,z_0), \qquad (2.3)$$

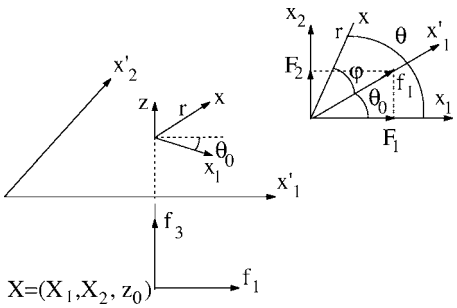

FIG. 3. Configuration for the calculation of the Green's tensor: the horizontal force f_1 is along the x_1' direction, which forms an angle θ_0 with the x_1 direction. The vertical force f_3 is along the z direction. The inset shows the position of (x_1',x_2',z) with respect to (x_1,x_2,z), the independent variables for the Green's tensor in Eq. (2.3).

$$G_{33}^0(\mathbf{x},\mathbf{X};\omega) = \frac{1}{2\pi\mu}\int_0^\infty dk k \xi_L J_0(kr) g(k;z,z_0).$$

Figure 4 shows typical patterns of the Green's tensor components G_{3k}^0 $(k=1,2,3)$ visualized on the free surface, $z=0$.

III. INTERACTION OF A SURFACE ACOUSTIC WAVE WITH A DISLOCATION

We now consider the interaction of a surface acoustic wave with a subsurface dislocation line. In the following sections, the expression of the scattered wave is given analytically and discussed further on the basis on numerical calculations. The results will be presented for configurations close to those of the experiments of Refs. 11–13, hereafter referred to as C_1: the incident wave has a frequency of 580 MHz and propagates in an elastic medium ($LiNbO_3$) with $c_T \simeq 3758$ m s^{-1}, $\gamma=2$, and $\rho=4.6\times10^3$ kg m^{-3}. The Rayleigh wave has a 6 μm wavelength at this frequency. The subsurface dislocation line has a Burgers vector $b=0.55$ nm, a damping coefficient $B=10^{-5}$ Pa s, and length $2L$. Usual estimates for the drag coefficient B fall around 10^{-5} Pa s at room temperature, in rough agreement with various estimates $B \simeq 10^{-2}\ \mu b/c_T$ (Refs. 26–28) (this estimation comes from the expression of B above the Debye temperature: $B \simeq kT\omega_D^2/\pi^3 c_T^3$, with k the Boltzmann constant, $\omega_D \simeq c_T\pi/b$ the Debye frequency, and T the temperature, and taking $\mu b^3 \simeq 1$ eV, an estimate valid for most materials). We shall use $m=\rho b^2$ (the dislocation mass per unit length) and $\Gamma = mc_T^2$ (the dislocation line tension). These expressions are expected to be valid in the subsonic regime (see, for instance, Ref. 29 in deriving the equation of motion for dislocation submitted to an external stress).

A. Theoretical calculations

The configuration we are interested in is illustrated in Fig. 5. An incident Rayleigh wave, with angular frequency ω, is generated at the free surface of a semi-infinite elastic medium. The medium contains in its bulk an isolated edge dislocation line. The line can have any direction, but we assume it does not touch the free surface.

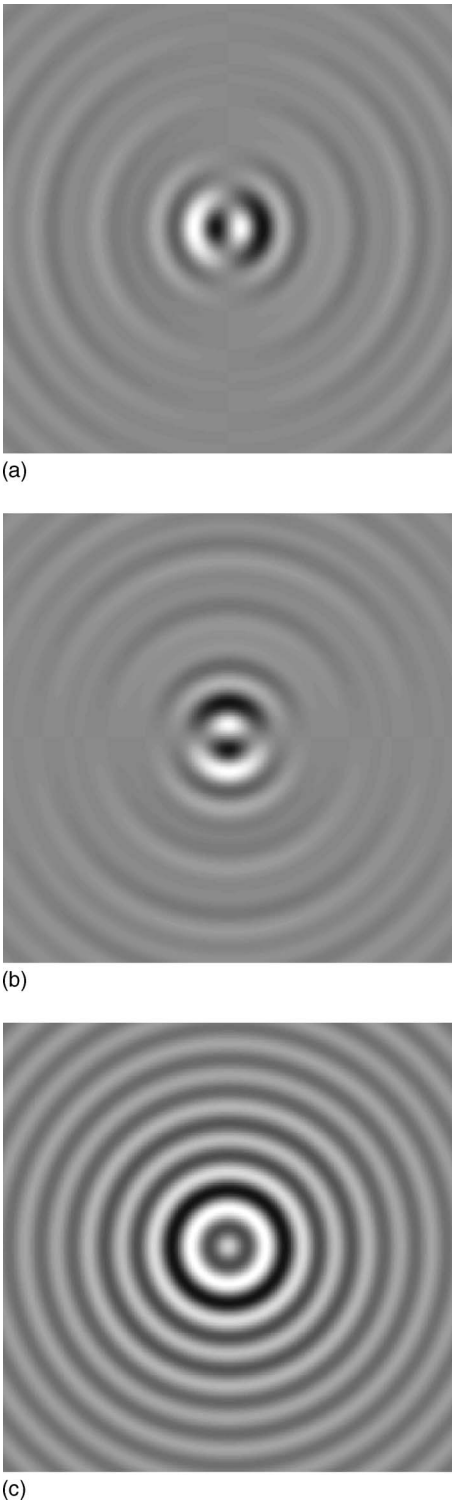

FIG. 4. Components of the Green's tensor $G_{3k}^0(\mathbf{x},\mathbf{X};\omega)$ for $\mathbf{x}$ on the free surface $(z=0)$ and $z_0=-\lambda_R$: (a) G_{31}^0, (b) G_{32}^0, and (c) G_{33}^0. Calculations are performed with the same values of ρ, c_T, c_L, and ω as in Fig. 2.

A qualitative model for the interaction of an acoustic wave with many dislocations in an infinite medium has been known, in terms of a coherent wave description, since the

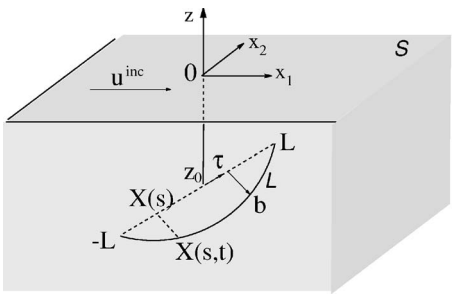

FIG. 5. An incident surface wave interacts with a subsurface dislocation line.

work of Granato and Lücke (see, e.g., Ref. 2), and the literature on the subject is vast. The quantitative modeling of the interaction with a single dislocation is, however, more recent[6,7] and the mechanism of this interaction can be viewed as a two-step process: the incident wave produces an external stress on the dislocation that oscillates in response. The oscillating dislocation emits an outgoing, scattered wave that superposes with the incident wave. The basic equations to treat the problem are the following. The equation

$$m\ddot{X}_k(s,t) + B\dot{X}_k(s,t) - \Gamma X_k''(s,t) = F_k(t) \tag{3.1}$$

describes the equation of motion for the dislocation line, where $\mathbf{X}(s,t)$ is the position vector along the line, $m \simeq \rho b^2$ is the dislocation mass per unit length, $\Gamma \simeq \rho b^2 c_T^2$ its line tension, B the drag coefficient, and $F_k = \epsilon_{kjm}\tau_m b_i \sigma_{ij}$ the Peach-Koehler force (ϵ_{ijk} denotes the usual completely antisymmetric tensor) that accounts for the external loading. We consider a dislocation line that is pinned at its ends, so the appropriate boundary conditions are $X_k(\pm L,t)=0$. The dislocation is assumed to be a gliding edge dislocation, so its motion $\mathbf{X}$ occurs along the direction of the Burgers vector. We denote $\mathbf{t}$ this direction, with $\mathbf{b}=b\mathbf{t}$, $\boldsymbol{\tau}$ the unit tangent along the dislocation line, and $\mathbf{n} \equiv \boldsymbol{\tau} \times \mathbf{t}$.

The wave is described by a displacement vector $\mathbf{u}$ that is a solution of the wave equation

$$\rho \partial_{tt} u_i(\mathbf{x},t) - c_{ijkl}\partial_{x_j}\partial_{x_l} u_k(\mathbf{x},t) = 0,$$

with two boundary conditions: (1) Displacement is multivalued with a discontinuity equal to the Burgers vector when crossing a time-dependent surface $S(t)$ that abuts at the (moving) dislocation line $\mathcal{L}(t)$: $[u_i]_{S(t)}=b_i$, while stress is single valued: $[c_{ijkl}(\partial u_l/\partial x_k)n_j]_{S(t)}=0$; and (2) normal stress vanishes at the free surface S, defined by $z=0$: $[c_{ijkl}(\partial u_l/\partial x_k)n_j]_S=0$.

The solution for the time derivative of the wave displacement $\mathbf{v}=\dot{\mathbf{u}}$, the particle velocity, can be written in the form of a convolution with a source localized along the loop, an expression first given in Ref. 30, see also Ref. 9,

$$v_z^s(\mathbf{x},t) = \epsilon_{jnh} c_{ijkl} \int_{\mathcal{L}} \int dt'\, ds b_i \dot{X}_n(s,t')\tau_h \times \frac{\partial}{\partial X_l} G_{3k}^0[\mathbf{x},\mathbf{X}(s);t-t'], \tag{3.2}$$

where G^0 is the Green's function of the half space with a free surface. We shall call v_z^s the scattered wave when $\dot{X}$ is given by the response of the dislocation to the incident Rayleigh wave. That is, when X is the solution of Eq. (3.1) with a right-hand side given by the stress associated with the incident surface wave. We neglect the back reaction of the scattered wave on the dislocation dynamics.

In the expression above, it has been assumed that the dislocation oscillates with amplitude small compared to wavelength, so that its time-dependent position can be replaced by the static, equilibrium position $\mathbf{X}(s,t) \simeq \mathbf{X}(s)$, with $\mathbf{X}(s)=(0,0,z_0)+s\boldsymbol{\tau}$ $(-L \leqslant s \leqslant L)$. Also, since $\dot{X}_n(s)=\dot{X}(s)t_n$ for a gliding motion, we have $\epsilon_{jnh}t_n\tau_h=-n_j$. In the frequency domain, Eq. (3.2) becomes

$$v_z^s(\mathbf{x},\omega) = -\mu b \int_{\mathcal{L}} ds \dot{X}(s,\omega) \mathsf{M}_{lk} \frac{\partial}{\partial X_l} G_{3k}^0[\mathbf{x},\mathbf{X}(s);\omega], \tag{3.3}$$

where we have defined $\mathsf{M} \equiv \mathbf{n}\,{}^t\mathbf{t} + \mathbf{t}\,{}^t\mathbf{n}$ and we have used $c_{ijkl}t_i n_j = \mu \mathsf{M}_{lk}$. The next step in the calculation of v_z^s in Eq. (3.3) is the determination of $\dot{X}(s,\omega)$ and of $\partial_{X_l} G_{3k}^0(\mathbf{x},\mathbf{X};\omega)$. This is done in the next two sections.

1. Motion of the dislocation line: $\dot{X}(s,\omega)$

The response of the dislocation depends on the incident wave. The displacements associated with an incident surface acoustic wave propagating along the x_1 direction are

$$u_1^{inc}(\mathbf{x},\omega) = (k_R A e^{\nu_L z} + \nu_T e^{\nu_T z}) e^{ik_R x_1},$$
$$u_z^{inc}(\mathbf{x},\omega) = -i(\nu_L A e^{\nu_L z} + k_R e^{\nu_T z}) e^{ik_R x_1}, \tag{3.4}$$

where $A \equiv -2\sqrt{1-\zeta^2}/(2-\zeta^2)$, ζ is the zero of the Rayleigh polynomial $P(\zeta)=\zeta^6-8\zeta^4+8\zeta^2(3-2/\gamma^2)-16(1-1/\gamma^2)$, and $\nu_{L,T} \equiv \sqrt{k_R^2 - k_{L,T}^2} > 0$.

In Eq. (3.1), the Peach-Koehler force $\mathbf{F}=F\mathbf{t}$ is written considering the external resolved shear stress σ generated by the incident wave at the dislocation position $\mathbf{X}(s)$: $F=\sigma b$, where σ can be written in a gliding motion $\sigma = \mathsf{M}_{lk}\partial_{x_l} u_k^{inc} = 2n_1 t_1 \partial_{x_1} u_1^{inc} + 2n_3 t_3 \partial_z u_z^{inc} + (n_1 t_3 + n_3 t_1)(\partial_{x_1} u_z^{inc} + \partial_z u_1^{inc})$. This means that the problem is solved in a first Born approximation, implying small scattering strength. In the frequency domain, we have to solve

$$X''(s,\omega) + K^2 X(s,\omega) = -\frac{1}{\Gamma} F(s,\omega) = -[C_L(\omega) e^{\alpha_L s} + C_T(\omega) e^{\alpha_T s}], \tag{3.5}$$

with $K \equiv \sqrt{(m\omega^2 + iB\omega)/\Gamma}$,

$$C_L \equiv 2\frac{\mu b}{\Gamma} A e^{\nu_L z}[i(n_1 t_1 k_R^2 - n_3 t_3 \nu_L^2) + (n_1 t_3 + n_3 t_1) k_R \nu_L], \tag{3.6}$$

$$C_T \equiv \frac{\mu b}{\Gamma} e^{\nu_T z}[2i(n_1 t_1 - n_3 t_3)k_R \nu_T + (n_1 t_3 + n_3 t_1)(k_R^2 + \nu_T^2)],$$

and $\alpha_{L,T} \equiv \nu_{L,T}\tau_3 + ik_R\tau_1$. Also, in Eq. (3.6), z means $z_0 + s\tau_3$, the depth of the dislocation point whose parameter is s. The solution is

$$X(s,\omega) = \frac{C_L}{\alpha_L^2 + K^2}\left[e^{\alpha_L s} - \frac{\cosh \alpha_L L}{\cos KL}\cos Ks - \frac{\sinh \alpha_L L}{\sin KL}\sin Ks\right] + \frac{C_T}{\alpha_T^2 + K^2}\left[e^{\alpha_T s} - \frac{\cosh \alpha_T L}{\cos KL}\cos Ks - \frac{\sinh \alpha_T L}{\sin KL}\sin Ks\right], \quad (3.7)$$

and the dislocation velocity is $\dot{X}(s,\omega) = -i\omega X(s,\omega)$.

2. Gradient of the Green's tensor

The spatial derivatives of the Green's tensor that we need for our application to dislocation and/or sound interaction are given here with the same notation used in Sec. II C, and they are evaluated for $\mathbf{x}$ on the free surface ($z=0$). We simply use $\partial_{X_1} = -(\cos\theta)\partial_r + [(\sin\theta)/r]\partial_\theta$ and $\partial_{X_2} = -(\sin\theta)\partial_r - [(\cos\theta)/r]\partial_\theta$ to get, from Eq. (2.3), $\partial_{X_j} G^0_{3i}$ $(1 \leqslant i,j \leqslant 3)$

$$\partial_{X_\cdot} G_{3\cdot}(\mathbf{x},\mathbf{X};\omega) = \frac{1}{4\pi\mu}\begin{pmatrix} -I_{f_0}(r) + (\cos 2\theta) I_{f_2}(r) & (\sin 2\theta) I_{f_2}(r) & (2\cos\theta) I_{f_{z1}}(r) \\ (\sin 2\theta) I_{f_2}(r) & -I_{f_0}(r) - (\cos 2\theta) I_{f_2}(r) & (2\sin\theta) I_{f_{z1}}(r) \\ (2\cos\theta) I_{g_1}(r) & (2\sin\theta) I_{g_1}(r) & 2 I_{g_{z0}}(r) \end{pmatrix}, \quad (3.8)$$

where

$$I_{f_0}(r) \equiv \int dk k^3 J_0(kr) f(k),$$

$$I_{f_2}(r) \equiv \int dk k^3 J_2(kr) f(k),$$

$$I_{g_1}(r) \equiv \int dk k^2 \xi_L J_1(kr) g(k),$$

$$I_{f_{z1}}(r) \equiv \int dk k^2 J_1(kr) \partial_{z_0} f(k), \quad (3.9)$$

$$I_{g_{z0}}(r) \equiv \int dk k \xi_L J_0(kr) \partial_{z_0} g(k),$$

$$f(k) = [(k_T^2 - 2k^2)e^{\xi_L z_0} + 2\xi_L \xi_T e^{\xi_T z_0}]/F(k),$$

$$g(k) = [(k_T^2 - 2k^2)e^{\xi_L z_0} + 2k^2 e^{\xi_T z_0}]/F(k),$$

and where ∂_{z_0} denotes the derivative with respect to z_0. The spatial derivatives $\partial_{X_j} G^0_{3i}$ are numerically calculated as described in Sec. II B, and we simply evaluate then

$$\mathsf{M}_{lk}\partial_{X_l} G^0_{3k} = \sum_{i,j} n_i t_j (\partial_{X_j} G^0_{3i} + \partial_{X_i} G^0_{3j}) \quad (3.10)$$

for $\mathbf{X}(s) = (s\tau_1, s\tau_2, z_0 + s\tau_3)$, with $-L \leqslant s \leqslant L$ and $\mathbf{x} = (x_1, x_2, 0)$ on the free surface.

B. Simplified expression in the case of a short dislocation line parallel to the free surface

In order to obtain a second validation of our numerical procedure, we now use it to compute a simple situation that is also amenable to analytical treatment, and compare both. The simplified situation is characterized by the following: (1) the dislocation line and the Burgers vector are parallel to the free surface. This implies $\mathbf{n} = (0,0,1)$ and $(\boldsymbol{\tau}, \mathbf{t})$ is deduced from $(\mathbf{x}_1, \mathbf{x}_2)$ by a rotation of angle α, see Fig. 6 below, with $\xi = 0$. (2) The length of the dislocation line L is small compared to the wavelength: $k_R L \ll 1$. (3) Far-field radiation is considered, where the contribution of the Rayleigh wave is expected to be dominant: $k_R r \gg 1$. Under these conditions, the expressions for $v^s(\mathbf{x},\omega)$ simplify to

$$v_z^s(\mathbf{x},\omega) = -2\mu b^2 \sin\alpha \sin(\theta - \alpha) f_1(\omega) f_2(z_0) f_3(L) \times H_1^{(2)}(-k_R r), \quad (3.11)$$

where $f_1(\omega) \equiv \omega k_R^2 \nu_L (k_T^2 - 2k_R^2)/[F'(k_R)(m\omega^2 + i\omega B)]$, with $F'(k_R) = -8k_R(k_T^2 - 2k_R^2) - 4k_R[2\nu_L^2\nu_T^2 + k_R^2(\nu_L^2 + \nu_T^2)]/(\nu_L\nu_T)$,

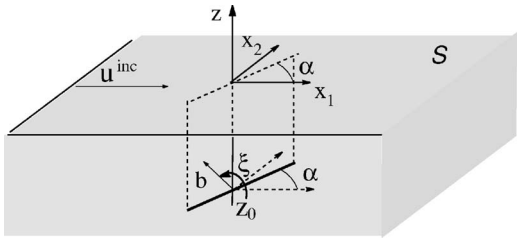

FIG. 6. Configuration of a dislocation line parallel to the free surface. The dislocation line is $2L$ long, at depth z_0, and is at an angle α with the x_1 direction.

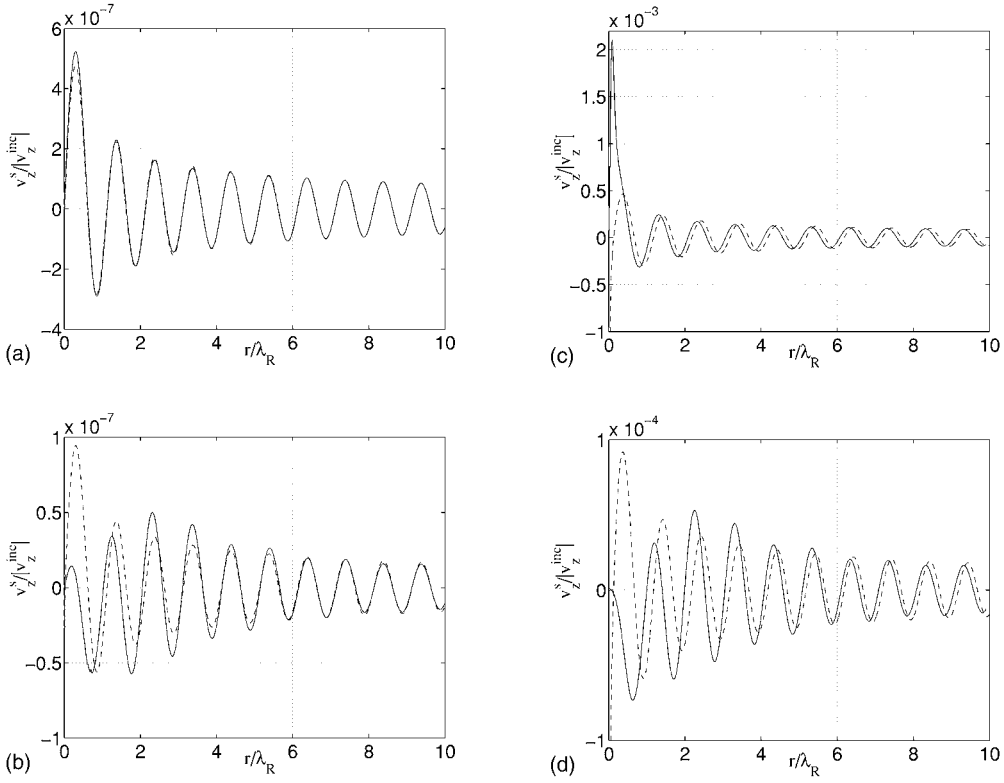

FIG. 7. Comparison between the forward-scattered elastic velocity calculated numerically $v_z^s(r,\theta=0)$ with the (simplified) analytical expression in Eq. (3.11). Full lines correspond to the numerical calculation and dashed lines to the analytical expression. Calculations are performed in the configuration C_1 with $\alpha=\pi/7$ and with (upper panels), $L=\lambda_R/100$ for (a) $z_0=-\lambda_R/10$ and (b) $z_0=-\lambda_R$ and with (lower panels), $L=\lambda_R/10$ for (c) $z_0=-\lambda_R/10$ and (d) $z_0=-\lambda_R$.

$f_2(z_0)\equiv(2k_R^2-k_T^2)(e^{\nu_L z_0}-e^{\nu_T z_0})^2$ (where we have used $2\nu_L k_R A=k_T^2-2k_R^2$), and $f_3(L)\equiv L[1-\tan(KL)/(KL)]$. $H_1^{(2)}$ denotes the Hankel function of second kind and of order 1. This expression is *a priori* valid only in the far field but, as seen previously for the Green's function, when $|k_R z_0|$ is small enough, that is, when the dislocation line is near the free surface, it gives a reasonable approximation of the field, as illustrated in Fig. 7.

C. Scattered waves and interference pattern on the free surface

We give here some pictures of the fields that are produced by dislocation line scattering in a configuration C_1 described at the beginning of this section: The dislocation line is parallel to the free surface, with α the angle that it forms with the x_1 direction, the direction of incidence (Fig. 6). The Burgers vector is perpendicular to the dislocation line and the angle ξ gives its direction with the horizontal.

In order to facilitate a comparison with the experiments of Refs. 11–13, we plot the displacement $u_z^s=v_z^s/(-i\omega)$ rather than the velocity v_z^s. Figure 8 shows the wave $u_z^s(\mathbf{r},z=0)$ scattered by a short edge dislocation line $L=\lambda_R/10$ with a Burgers vector parallel or perpendicular to the free surface, visualized on the free surface. The expression for a Burgers vector parallel to the free surface is given in the "far field" by Eq. (3.11) and, as expected, extinctions are observed in the direction $\theta=\alpha$ and $\theta=\alpha+\pi$ (i.e., here, $\theta=\pi/2$ and $\theta=3\pi/2$).

Figure 9 shows the scattered fields for long dislocation lines ($L=10\lambda_R$) parallel to the free surface with Burgers vector parallel to the free surface for three different line orientations α with respect to the incident wave direction (along the horizontal axis on the figures). The amplitudes of the scattered wave and of the dislocation motion are indicated. It can be seen that the dislocation motion has an increasing amplitude when the line lies perpendicular to the incident direction, resulting in an increase of the scattering strength. This is also the case for a short dislocation line, with a sin α dependence as shown in Eq. (3.11). For short lines, the pattern of the scattered wave rotates with α and its amplitude scales as sin α. This is because the response of the dislocation keeps the same form, given by its fundamental mode of oscillation, with an amplitude that depends on the incident wave direction. For long dislocation lines, the response of the dislocation is more complex. When the line is parallel to the incident wave direction, the dislocation line oscillates with the periodicity of the incident wavelength. Conversely, when the line is perpendicular to the direction of the incident wave, all points of the line receive an excitation with the same phase. In any case, whatever the length of the disloca-

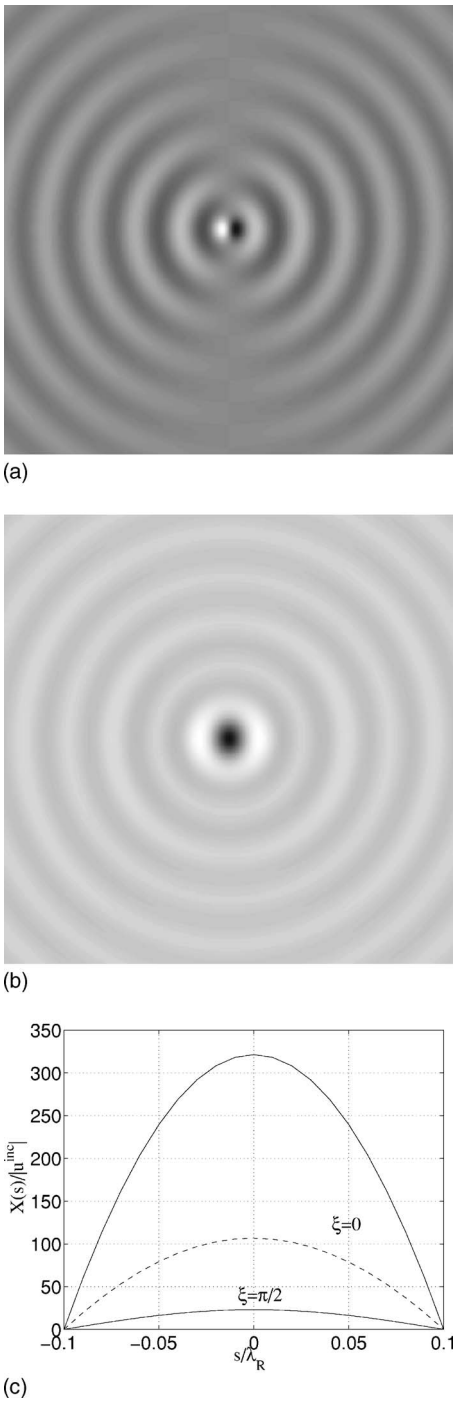

FIG. 8. Scattered displacement fields u_z^s for a dislocation line (with $2L=\lambda_R/5$) parallel to the free surface ($\alpha=\pi/2$) at depth $z_0=-2/k_R$. The box is a square $10\lambda_R$ on each side. The Burgers vector is (a) parallel to the free surface, $\xi=0$ (we get $|u_z^s|/|u_z^{inc}|\sim 10^{-1}$), and (b) perpendicular to the free surface, $\xi=\pi/2$ (we get $|u_z^s|/|u_z^{inc}|\sim 9.10^{-2}$). (c) Full line, corresponding motions of the dislocation line $X(s)$; dotted line, the motion of the dislocation line for $\xi=0$ and $\alpha=\pi/9$ (the amplitude of motion would be zero for $\alpha=0$). ξ denotes the angle between the incident wave direction (x_1 direction) and the Burgers vector. See Sec. III D for the definition of scattering strength $|u_z^s|/|u_z^{inc}|$.

tion line, the amplitude of the line motion increases from $\alpha=0$ to $\alpha=\pi/2$.

Finally, Fig. 10 shows the interference pattern $u_z^{inc}(\mathbf{x})+u_z^s(\mathbf{x})$ on the free surface in the configuration described in Ref. 13: three dislocation lines are parallel to the free surface (we assume the Burgers vector is parallel to the free surface too, as in Ref. 13) and they form a rather small angle $\alpha<20°$ with the direction of the incident wave. A zoom near one line is given to visualized the near field. Both pictures are qualitatively in good agreement with those of the experiments. In order to advance on quantitative aspects, there are a number of experimental questions whose answers would be of value in order to enhance x-ray imaging as a nonintrusive tool to study the wave-dislocation interaction.

(1) Dependence on the line length. The dislocation lines that are visualized in the experiments are quite long. At the working frequency, it is probably not possible to visualize the scattering by short dislocation lines since the scattering strength will be much smaller. Is it possible to check if a threshold is experimentally detected depending on the line length?

(2) Dependence on the dislocation line orientation. The interference pattern is here given for small angle α, while the present theory predicts an increasing scattering strength for increasing α. Is it possible to experimentally observe this dependence?

(3) Dependence on line depth. The scattering strength is expected to be strongly dependent on the depth z_0 of the subsurface dislocation line, as will be discussed in the forthcoming section. Briefly speaking, scattering at a given frequency is particularly strong at a given depth. Thus, the dislocation lines responsible for the scattering observed by Zolotoyabko *et al.*[11] and Shilo and Zolotoyabko[12,13] must be at the depth corresponding to their working frequency. Is it possible to check this point by a change of frequency and/or line depth?

In this configuration, we obtain amplitudes of the motion of the dislocation lines typically of order $X\sim 500u_z^{inc}$ [this is also the order of magnitude observed in Figs. 8(c) and 9(d)]. In the experiments of Ref. 13, $u_z^{inc}\sim 0.05$ nm (deduced from the incident strain experimentally measured), and we thus evaluate the amplitude of the dislocation motion to be $X\sim 25$ nm. Note that this is very small compared to the wavelength $\lambda\sim 6$ μm of the Rayleigh wave, thus validating the assumption made in Sec. III A. This also gives the dislocation velocity around 90 m s^{-1}, well below the speed of sound. This is further discussed in the following section.

1. Comment on the calculation of Ref. 13

The interference pattern observed in Ref. 13 was interpreted by Shilo and Zolotoyabko using a calculation that certainly captures the essence of the interaction between the incident wave and the dislocation, and it is of interest to compare their approach to ours. Their approach is as follows: the vertical displacement field is assumed to follow the movement of the dislocation, with the latter movement being induced, as in our approach, by the presence of the incident wave. The displacement field is thus written as $U_z(\mathbf{x}-\mathbf{X})$, where $\mathbf{X}$ is the time-dependent position of the dislocation

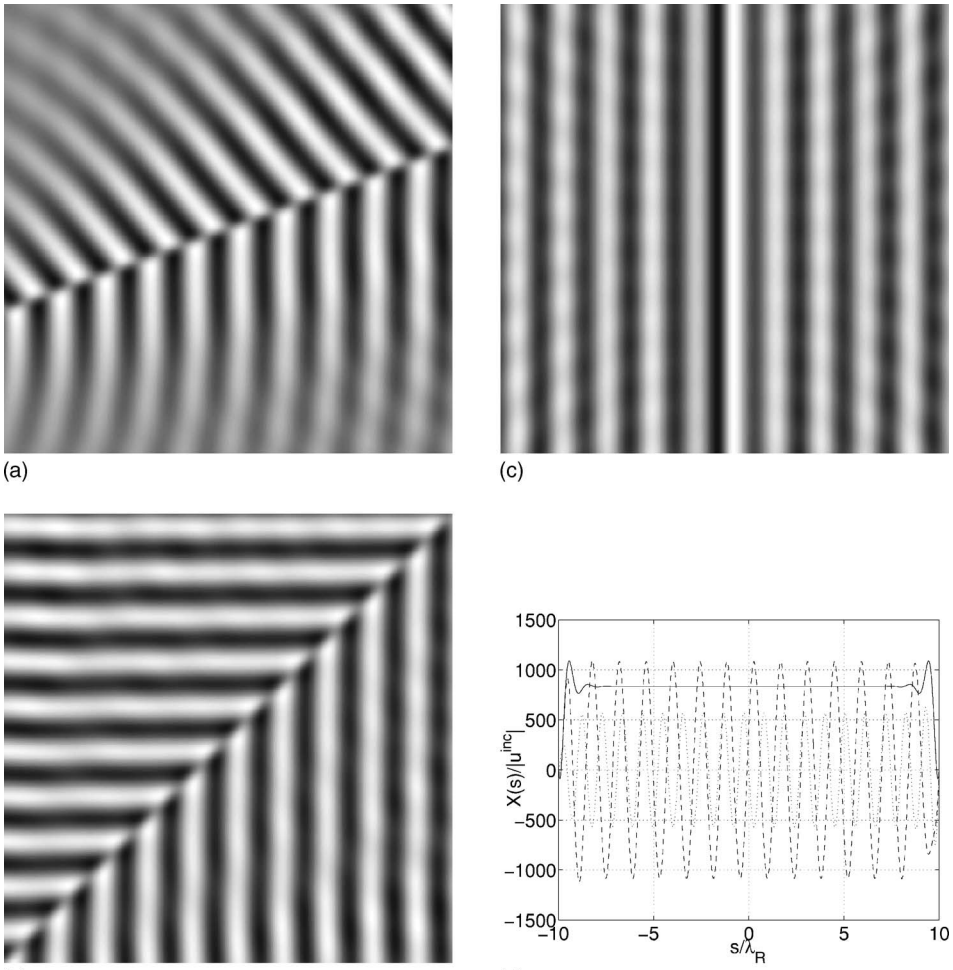

FIG. 9. Scattered fields for $L=10\lambda_R$, $\xi=0$, the line is parallel to the free surface at depth $z_0=-2/k_R$ (the box is $10\lambda_R$ on each side) and (a) $\alpha=\pi/9$ (we get $|u_z^s|/|u_z^{inc}|\sim 0.6$), (b) $\alpha=\pi/4$ (we get $|u_z^s|/|u_z^{inc}|\sim 1$), and (c) $\alpha=\pi/2$ (we get $|u_z^s|/|u_z^{inc}|\sim 1.5$). (d) Corresponding motion of the dislocation line $X(s)$: full line, $\alpha=\pi/2$; dashed line, $\alpha=\pi/4$; and dotted line, $\alpha=\pi/9$. See Sec. III D for the definition of scattering strength $|u_z^s|/|u_z^{inc}|$.

and $U_z(\mathbf{x})$ is the static displacement around the dislocation (in Ref. 13, the two-dimensional case is considered, a simplification that may be valid close enough to the dislocation line). The scattered field is then defined as the difference between the static field induced by the moving dislocation and the static field induced by the dislocation at rest and for a dislocation motion along the x_2 direction (the line is infinite along the x_1 direction with the Burgers vector along x_2):

$$u_z^s(x_1,x_2,z;t)=U_z(x_2-X(x_1,t),z)-U_z(x_2,z), \quad (3.12)$$

with

$$U_z(x_2,z)=-\frac{b}{8\pi(1-\nu)}\left[(1-2\nu)\log(x_2^2+z^2)+\frac{x_2^2-z^2}{x_2^2+z^2}\right], \quad (3.13)$$

with $\nu\equiv\lambda/[2(\lambda+\mu)]$ the Poisson ratio. Note that the expression of U_z used in Ref. 13 coming from Nabarro[31] differs from the expression given by Landau and Lifshitz[22] by an additive constant that does not affect our calculations. For small amplitude of the dislocation motion, u_z^s simplifies to $u_z^s(x_2,z;t)=X(x_1,t)\partial_{x_2}U_z(x_2,z)$, from which we deduced the scattered velocity field $v_z^s=\dot{u}_z^s$ as a function of $\dot{X}$ (dot means time derivative) in the frequency domain:

$$v_z^s(x_1,x_2,z;\omega)=\dot{X}(x_1,\omega)\frac{\partial}{\partial x_2}U_z(x_2,z). \quad (3.14)$$

This expression of v_z^s has to be compared with the expression given by our theory under the same approximations. This means that (1) the line is assumed to be infinite and the presence of the free surface is omitted, and (2) the static field can be used if the frequency goes to zero or, equivalently, in the near-field approximation: $k_{\alpha,\beta}r\ll 1$. In this case, the integral representation in Eq. (3.3) becomes

$$v_z^s(x_1,x_2,z;\omega)=\mu b\dot{X}(x_1,\omega)\left[\frac{\partial}{\partial x_2}g_{33}^0(x_2,z,;\omega)+\frac{\partial}{\partial z}g_{32}^0(x_2,z;\omega)\right], \quad (3.15)$$

where we have denoted $g^0(x_2,z;\omega)\equiv\int dsG^0(s,x_2,z;\omega)$ the two-dimensional Green's tensor in infinite space and where we have used $\mathsf{M}_{lk}=\delta_{l2}\delta_{k3}+\delta_{l3}\delta_{k2}$. Note that the origin is here at the dislocation position (at rest). Note also that it has been assumed that the dislocation velocity $\dot{X}$ can be taken out of the integral, a simplification that may be valid close enough to the dislocation line.

The assumption that the static field can be used is now taken into account by using the static Green's function

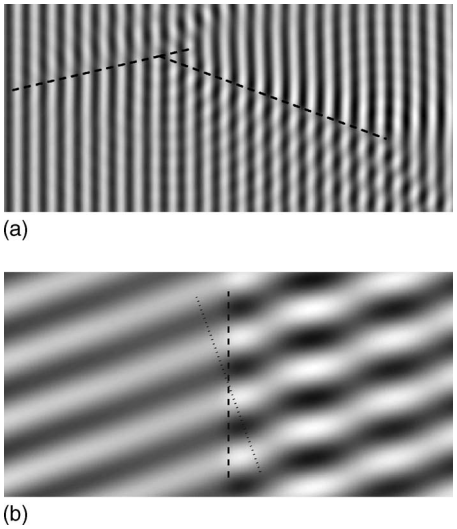

FIG. 10. Interference patterns calculated in a configuration similar to those described in Ref. 13: an incident wave at frequency $\omega=(2\pi)(580\times10^6)$ rad s^{-1} propagates in a medium (configuration C_1) containing in its bulk three dislocation lines (dotted line on the figure), forming a rather small angle with the direction of the incident wave. The characteristics of the dislocations lines are, from left to right, $2L_1=9\lambda_R$, $\alpha_1=58°$ (that is, 13° with $-x_1$ axis); $2L_2=\lambda_R$; $\alpha_2=13°$; and $2L_3=7\lambda_R$, $\alpha_3=-20°$. All dislocations are assumed to be at $z_0=-3/k_R$. (a) Interference pattern calculated in a box $26\lambda_R\times12\lambda_R$ (to be compared with Fig. 1(a) in Ref. 13). (b) Wave distortion in the vicinity of the vibrating dislocation. The box is $8\lambda_R\times4\lambda_R$ (the direction of the dislocation line is indicated by dashed line and the direction of the incident wave by dotted line), to be compared with Fig. 3 in Ref. 13.

$g^0_{ab}(x_2,z)$ $(a,b=2,3)$ instead of the dynamic one,[32]

$$g^0_{ab}(x_2,z)=\frac{1}{4\pi\mu}\left[\delta_{ab}\frac{\lambda+3\mu}{\lambda+2\mu}(\log x+\mathcal{D})-\frac{\lambda+\mu}{\lambda+2\mu}\frac{x_a x_b}{x^2}\right], \tag{3.16}$$

where $\mathcal{D}$ is a constant expressed as a function of a cutoff distance; it takes care of the divergence of the integral that defines the Green's function. To compare the expression of the scattered fields in Eqs. (3.14) and (3.15), it is sufficient to compare $\partial_{x_2}U_z$ with $\mu b[\partial_{x_2}g^0_{33}+\partial_z g^0_{32}]$. It is easy to see that the two terms are equal, from which we deduce that the two approaches indeed focus on the same mechanism. Actually, the calculation of Ref. 13 can be recovered from our calculation.

The main improvement in our theory is to account for the presence of the free surface. In addition, we also account for the finite length of the dislocation line, and our dynamical calculation holds in the whole half space, not just in the near field. All these modifications lead to an increase in the intensity of the emitted field with respect to the static field used in Ref. 13. In the experimental configuration that we mimic in the previous section, we found a 2 orders of magnitude increase. Thus, we obtain similar interference pattern with a ratio X/λ_R 2 orders of magnitude smaller than in Ref. 13. This has two important consequences: (1) The drag coefficient B falls in the usual range $B\simeq10^{-5}$ Pa s and (2) the dislocation moves in a subsonic motion with $\dot{X}/c\simeq10^{-2}$. Had this ratio been higher, the equation of motion would have had to be modified to take into account the Lorenz force (see, for instance, Ref. 29).

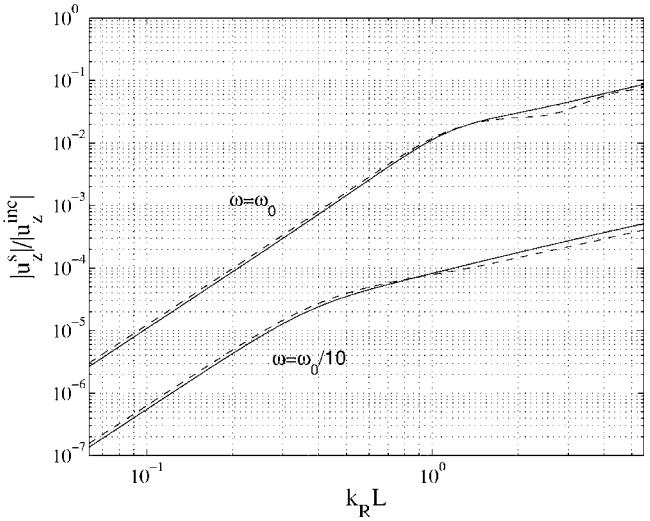

FIG. 11. Scattering strength $|u_z^s|/|u_z^{inc}|$ as a function of the length $2L$ of the dislocation line. The configuration is C_1 with a line parallel to the free surface (the Burgers vector also) forming an angle $\alpha=\pi/9$ with the direction of the incident wave and $z_0=-1.5/k_{R0}$. Full lines, analytical (simplified) expressions in Eq. (3.11); dashed lines, numerical calculations.

We conclude that the unexpectedly high value of the dislocation velocity and the unusual low value of the drag coefficient B announced in Ref. 13 are artifacts of the approximations in the model therein.

D. Discussion on the scattering strength

The scattering strength can be measured as $|u_z^s|/|u_z^{inc}|$, where $|u^s|$ denotes a typical amplitude, to be defined, of the

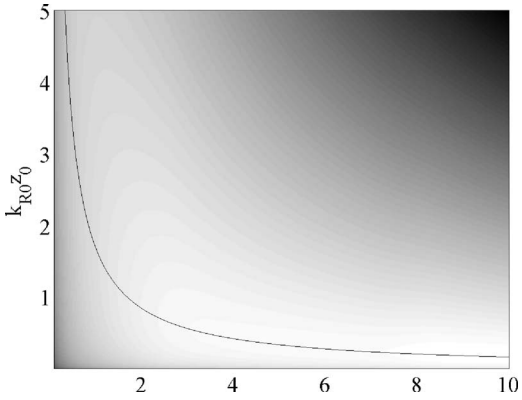

FIG. 12. Scattering strength $|u_z^s|/|u^{inc}|$ (gray scales correspond to logarithm values) as a function of z_0 and ω deduced from the analytical expression in Eq. (3.11). The configuration is C_1 with the line and Burgers vector both parallel to the free surface. The line is at an angle $\alpha=\pi/9$ with the direction of the incident wave and has a length $2L=\lambda_{R0}/5$. The solid curve is a plot of the function $z_0k_{R0}=1.7(\omega/\omega_0)^{-1}$, indicating the position of the maximum scattering strength as z_0 varies for fixed frequency (vertical profiles).

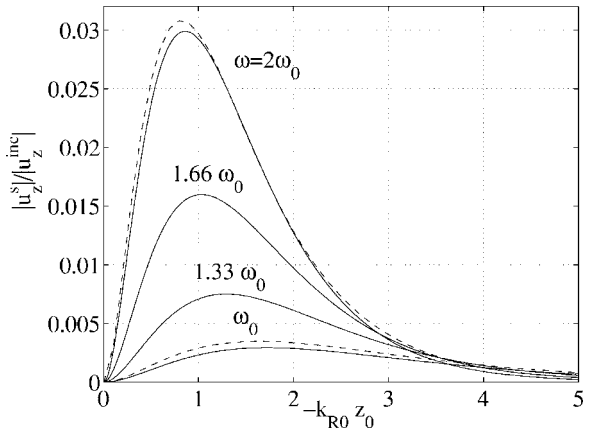

FIG. 13. Scattering strength $|u_z^s|/|u_z^{inc}|$ as a function of z_0 at difference frequencies ω (vertical cuts of Fig. 12). Full lines correspond to the analytical (simplified) expression, and dashed lines correspond to the numerical calculations with an adjusted scale.

secondary wave re-emitted by the dislocation and $|u^{inc}|$ the amplitude of the incident wave, both measured at the free surface. In this section, most of the results are calculated using the simplified expression in Eq. (3.11), and we define $|u^s|$ as the amplitude $\mathcal{A}$ of the Rayleigh wave in the far field $\mathcal{A}e^{ik_R r}/\sqrt{k_R r}$. For the results coming from numerical calculations, $|u^s|$ is taken as the mean value of the norm of u^s in a square box of $2\lambda_R$ large. This is an arbitrary definition but it has the advantage to consider the scattered amplitudes both in the near and in the far field. It has an adjustable scale factor, the size of the box. Of course, with decreasing z_0 values, it is expected that $|u^s|$ numerically loses physical meaning since the Born approximation diverges for $z_0=0$, $r=0$.

The scattering strength depends on the characteristics of the dislocation, notably b and B, but this dependence is not discussed here since most dislocation lines have $b\sim 0.5$ nm and $B\sim 10^{-5}$ Pa s. It also depends on the dislocation length $2L$, the depth of the dislocation z_0 and the frequency ω of the incident surface wave. These dependencies are discussed below. To do that, we use the frequency $\omega_0=(2\pi)(580\times 10^6)$ rad s^{-1} as a reference frequency and the Rayleigh wavelength λ_{R0} [associated with the Rayleigh wave number $k_{R0}\equiv\omega_0/(c_T\zeta)$] as a reference length. We explore L and z_0 around λ_{R0} and ω around ω_0.

Figure 11 shows the scattering strength as a function of the dislocation length L at ω_0 and $\omega_0/10$ frequencies. As previously seen, the scattering strength increases with increasing L. For small L, this dependence is as L^3 predicted in Eq. (3.11) by the function $f_3(L)$ and departs from this behavior for large L.

Figure 12 shows the scattering strength as a function of z_0 and ω using the simplified expression in Eq. (3.11). For each frequency ω, there is a maximum at $z_0k_R\simeq -1.7$. This is the maximum of the function $f_2(z_0)$, and it corresponds to the maximum reached by the incident stress σ that appears in the Peach-Koehler force as the force acting on the dislocation line. Such a maximum on the incident stress produces a maximum response of the dislocation line and thus of the amplitude of the scattered wave. This is illustrated further in

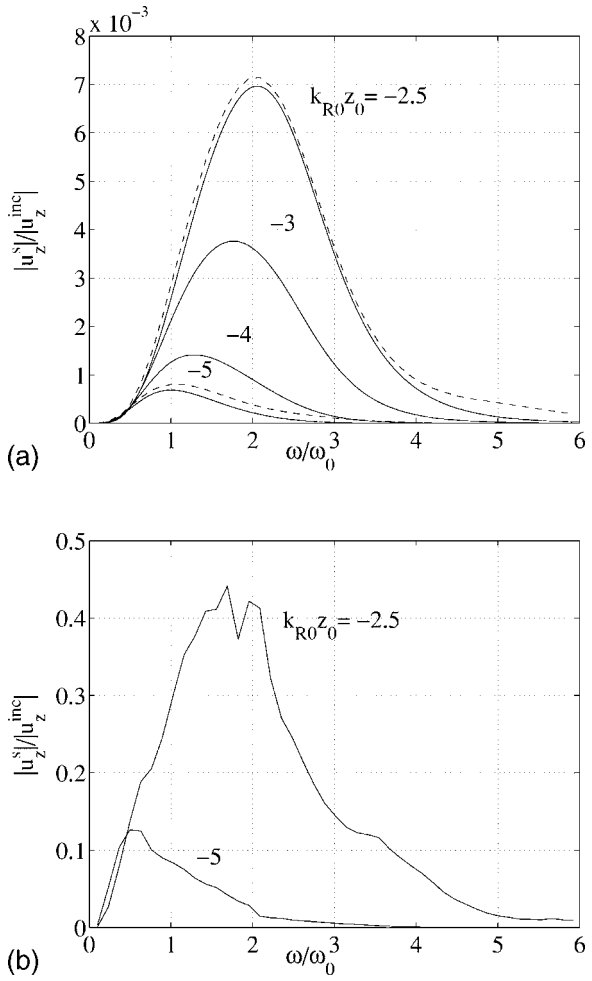

FIG. 14. Scattering strength $|u_z^s|/|u_z^{inc}|$ as a function of ω at different dislocation depths z_0. (a) Horizontal cuts of Fig. 12 for $L=\lambda_{R0}/10$: Full lines correspond to the analytical (simplified) expression and dashed lines correspond to the numerical calculations with an adjusted scale. (b) The curves correspond to numerical calculations for $L=10\lambda_{R0}$.

Fig. 13 that shows vertical cuts of the previous representation in Fig. 12, in agreement with numerical calculations. As expected, the numerical evaluation of the scattering strength is higher than the analytical one since the scattered amplitude is higher in the near field. For the readability of the figure, the values obtained from the numerical evaluation have been scaled by a constant factor.

Figure 14(a) shows the scattering strength as a function of ω (horizontal profiles of the previous representation in Fig. 12) and the comparison with numerical results for small L. It can be seen that, for a given depth of the dislocation line z_0, the scattering strength has a bandpass centered at a frequency satisfying $k_R\simeq -5/z_0$. This law, however, is only valid for z_0 deeper than around $-2/k_{R0}$. Numerical results for large L are shown in Fig. 14(b) and exhibit the same trend.

IV. CONCLUDING REMARKS

We have studied the interaction of a subsurface edge dislocation line of finite length with an incident surface acoustic

wave using a full three-dimensional vector approach. As an intermediate step, an efficient method for the numerical calculation of the Green's function for an elastic half space is developed. The main lesson we learn from this study is that, in order to get a quantitative appraisal of recent experiments that visualize vibrating dislocations, this full approach is a must. Further, having a powerful formalism at hand, a number of questions suggest themselves for experimental work that may lead to significant advances in the understanding of dislocation dynamics, a phenomenon that is at the root of many material properties.

The main approximation in our theory is the neglect of the secondary elastic waves on the dislocation dynamics, but we have relaxed the restrictions $\lambda_R \gg L$ of our previous work.[6,7] The derivations have been performed for an arbitrary orientation of the dislocation line, but results have been illustrated in the case of a line parallel to the free surface. The main motivation for this study was in the experiments of Shilo and Zolotoyabko, who are able to visualize the interference pattern between the incident wave and the scattered wave[11–13] and a part of the paper has been devoted to the comparison with Ref. 13. In cases close to the experimental configuration of Ref. 13, where $L \approx 10\lambda_R$ and depth $z_0 \approx -\lambda_R/\pi$, we find a scattering amplitude $|u_z^s|/|u_z^{inc}| \sim 0.5$ and thus an observable interference pattern.

ACKNOWLEDGMENTS

This work was performed under the auspices of ECOS-CONICYT Contract No. C04E01 and FONDAP Grant No. 11980002. F.B. gratefully acknowledges the support of FONDECYT Project No. 1060820 and ACT 15 (Anillo Ciencia y Tecnologia). Two of the authors (F.B. and F.L.) are pleased to thank Emil Zolotoyabko and Doron Shilo for fruitful discussions.

APPENDIX A: DERIVATION OF THE VERTICAL DISPLACEMENT DUE TO A SUBSURFACE POINT FORCE IN A SEMI-INFINITE ELASTIC MEDIUM

We have to solve

$$\rho\omega^2 u_i(\mathbf{x}) + c_{ijkl}\partial_j\partial_l u_k(\mathbf{x}) = -(f_1\delta_{i1} + f_3\delta_{i3})\delta(\mathbf{x}-\mathbf{X}), \tag{A1}$$

for $\mathbf{x}=(x_1,x_2,z\leqslant 0)$, with the boundary condition at the free surface, $z=0$, that the normal stress must vanish, $c_{i3kl}\partial_l u_k(\mathbf{x})_{|z=0} = 0$, and the radiation condition for $z\to-\infty$.

The system is solved using a two-dimensional Fourier transform on the horizontal coordinates, with $\mathbf{u}=(u_1,u_2,u_z)$ and $\mathbf{k}=(k_1,k_2)$. Denoting $U \equiv ik_1u_1 + ik_2u_2$, we get

$$0 \geqslant z \neq z_0 \begin{cases} [\mu\partial_{z^2} + \rho\omega^2 - (\lambda+2\mu)k^2]U(\mathbf{k},z) - (\lambda+\mu)k^2\partial_z u_z(\mathbf{k},z) = 0, \\ (\lambda+\mu)\partial_z U(\mathbf{k},z)[(\lambda+2\mu)\partial_{z^2} + \rho\omega^2 - \mu k^2]u_z(\mathbf{k},z) = 0, \end{cases} \tag{A2}$$

with the following conditions at $z=z_0$: $[\![U(\mathbf{k},z_0)]\!]=[\![u_z(\mathbf{k},z_0)]\!]=0$, $\mu[\![\partial_z U(\mathbf{k},z_0)]\!]=-ik_1f_1$, $(\lambda+2\mu)[\![\partial_z u_z(\mathbf{k},z_0)]\!]=-f_3$, where $[[\![H(z_0)]\!] \equiv \lim_{\epsilon\to 0} H(z_0+\epsilon) - H(z_0-\epsilon)]$, the free-surface boundary condition at $z=0$ that becomes $\lambda U(\mathbf{k},0) + (\lambda+2\mu)\partial_z u_z(\mathbf{k},0) = 0$, $\partial_z U(\mathbf{k},0) - k^2 u_z(\mathbf{k},0) = 0$, and the radiation condition for $z\to-\infty$. A solution (U,u_z) of the following form is sought:

$$0 \geqslant z \geqslant z_0 \begin{cases} U(\mathbf{k},z) = a_1 e^{\xi_L(z-z_0)} + a_2 e^{-\xi_L(z-z_0)} + b_1 e^{\xi_T(z-z_0)} + b_2 e^{-\xi_T(z-z_0)}, \\ u_z(\mathbf{k},z) = A_1 e^{\xi_L(z-z_0)} + A_2 e^{-\xi_L(z-z_0)} + B_1 e^{\xi_T(z-z_0)} + B_2 e^{-\xi_T(z-z_0)}, \end{cases}$$

$$z \leqslant z_0 \begin{cases} U(\mathbf{k},z) = a e^{\xi_L(z-z_0)} + b e^{\xi_T(z-z_0)}, \\ u_z(\mathbf{k},z) = A e^{\xi_L(z-z_0)} + B e^{\xi_T(z-z_0)}. \end{cases} \tag{A3}$$

Since in this paper we only need the vertical displacement for $z > z_0$ because the interest is in the surface displacement, we only have to determine (ξ_L,ξ_T) and (A_1,A_2,B_1,B_2). The resolution is straightforward and we get

$$\xi_{L,T} = \sqrt{k^2 - k_{L,T}^2}, \tag{A4}$$

$$A_1 = \frac{1}{2i\mu k_T^2}\{k_1 f_1[G(k)e^{\xi_L z_0} + 4\xi_L\xi_T(k_T^2 - 2k^2)e^{\xi_T z_0}] + i\xi_L f_3[G(k)e^{\xi_L z_0} + 4k^2(k_T^2 - 2k^2)e^{\xi_T z_0}]\}\frac{e^{\xi_L z_0}}{F(k)},$$

$$A_2 = \frac{1}{2i\mu k_T^2}[k_1 f_1 + i\xi_L f_3], \tag{A5}$$

$$B_1 = \frac{1}{2i\mu k_T^2}\left\{ k_1 f_1 [4k^2(k_T^2 - 2k^2)e^{\xi_L z_0} + G(k)e^{\xi_T z_0}] + i\xi_L f_3 \left[4k^2(k_T^2 - 2k^2)e^{\xi_L z_0} + G(k)\frac{k^2}{\xi_L \xi_T} e^{\xi_T z_0} \right] \right\} \frac{e^{\xi_T z_0}}{F(k)},$$

$$B_2 = -\frac{1}{2i\mu k_T^2}\left[k_1 f_1 + i\frac{k^2}{\xi_T} f_3 \right],$$

where $G(k) \equiv (k_T^2 - 2k^2)^2 + 4k^2 \xi_L \xi_T$ and $F(k) \equiv (k_T^2 - 2k^2)^2 - 4k^2 \xi_L \xi_T$. Letting $\mathbf{r} = (x_1, x_2)$, $\varphi \equiv (X_1, \mathbf{r})$, and $r \equiv |\mathbf{r}|$, $u_z(r, \varphi, 0 \leq z \leq z_0)$, we obtain

$$u_z(\mathbf{x}) = \frac{1}{2\pi\mu}\left[(\cos\varphi) f_1 \int dk k^2 J_1(kr) f(k,z) + f_3 \int dk k \xi_L J_0(kr) g(k,z) \right], \tag{A6}$$

with

$$2k_T^2 f(k,z) \equiv [G(k)e^{\xi_L z_0} + 4\xi_L \xi_T (k_T^2 - 2k^2)e^{\xi_T z_0}] \frac{e^{\xi_L z}}{F(k)} + [4k^2(k_T^2 - 2k^2)e^{\xi_L z_0} + G(k)e^{\xi_T z_0}] \frac{e^{\xi_T z}}{F(k)} + e^{-\xi_L (z - z_0)} - e^{-\xi_T (z - z_0)},$$

$$2k_T^2 g(k,z) \equiv [G(k)e^{\xi_L z_0} + 4k^2(k_T^2 - 2k^2)e^{\xi_T z_0}] \frac{e^{\xi_L z}}{F(k)} + \left[4k^2(k_T^2 - 2k^2)e^{\xi_L z_0} + \frac{k^2}{\xi_L \xi_T} G(k)e^{\xi_T z_0} \right] \frac{e^{\xi_T z}}{F(k)} + e^{-\xi_L (z - z_0)} - \frac{k^2}{\xi_L \xi_T} e^{-\xi_T (z - z_0)}, \tag{A7}$$

which is Eq. (2.1).

APPENDIX B: DETAILS ON THE NUMERICAL INTEGRATION

The numerical integration of the integrals in the Eq. (A6) presents several difficulties.

(1) Singularities are present on the real axis. As mentioned in the body of the text, this difficulty can be avoided by considering the elastic case as the limit of the viscoelastic case for small viscosity, adding a small imaginary part to the frequency. This moves the singularities off the real axis, so that the integration is possible. In practice, we have performed the numerical integration with $\omega(1 + i\epsilon)$, $\epsilon = 10^{-10}$. A Runge-Kutta method with adaptative step size has been used (Fig. 15) in a first interval $[0, k_0 = 1.5k_R]$ that contains the singularities (k_T, k_L, k_R), while the rest of the integral is treated as described below.

(2) Integrands oscillate because of the Bessel functions $J_n(kr)$. These functions are known to be difficult to integrate numerically for large r. References 23–25, 33, and 34 have proposed a Filon quadrature method to overcome this difficulty. The essentials of the method, as adapted to our expressions, are presented in Appendix C.

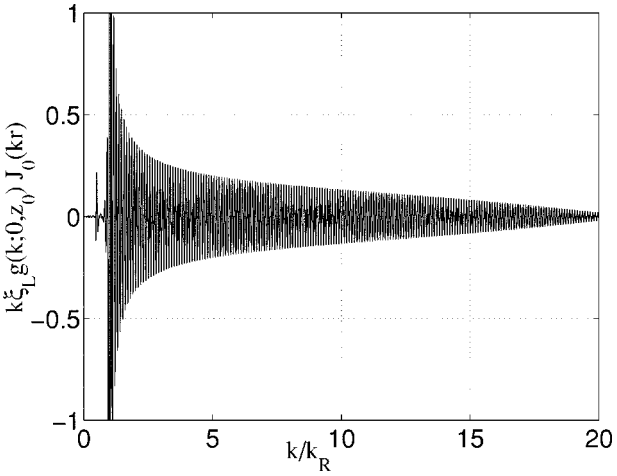

FIG. 15. Example of a curve to be integrated here in the integral that defines u_z in Eq. (A6) for $f_1 = 0$, $\epsilon = 10^{-10}$, $z_0 = \lambda_R/100$, and $r = 10\lambda_R$. Otherwise, $\omega = (2\pi)(580)\text{s}^{-1}$, $c_T = 3758\ \text{m s}^{-1}$, and $\gamma = 2$. In the interval $k/k_R = [0, 1.5]$, a usual Runge-Kutta method with adaptative step size is used. In the interval $k/k_R = [1.5, 10k_R|z_0|]$, a Filon quadrature method is used that avoids resolving the oscillation. The figure has been reduced: on the horizontal axis, the integration goes until $k_{\max}/k_R = 160$, and on the vertical axis, near the singularity $k = k_R$, the curve has a maximum close to 300.

(3) The last point is not a difficulty, but a criterion is needed to cut the upper limit of the integral and to choose the step size dk for the Filon quadrature method. When the Bessel terms are omitted, the form of the curves to be integrated is governed by the terms $e^{\nu_{L,T} z_0}$. Thus, we fix the step size for the Filon quadrature $dk = 1/(10|z_0|)$ and the upper limit of the integrals $k_{max} = k_0 + 10/|z_0|$.

APPENDIX C: THE INTEGRATION USING FILON AND/OR TRAPEZOIDAL SCHEME

1. Method

The Filon quadrature method has been developed in Refs. 23–25, 33, and 34. We remind here the basic ideas and formulas that we use and that to be found in those papers. The aim is to calculate integrals of the form $H(r) \equiv \int_a^b h(k) J_n(kr) dk$ for large r and smooth behavior of $h(k)$. The idea is to calculate by quadrature the integral using a discretization of $h(k)$ instead of a discretization on $h(k)J_n(kr)$, with the latter needing much more discretization points than the former. With $a = k_1$, $b = k_N$, and $k_j = a + (j - 1)\delta$ $[\delta \equiv 1/(N-1)]$, the discretized values of $h(k)$ are $h_j \equiv h(k_j)$. The idea is to develop h in a polynomial form on the interval $[k_j, k_{j+1}]$, since it is possible to derive and analytically evaluate the integrals $\int_{k_j}^{k_{j+1}} k^m J_n(kr) dk$.

For our application in the calculations in Eq. (3.8), we need $H(r)$ for $n = 0, 1, 2$ [the case $n = 2$ is deduced from $n = 0, 1$ using $J_2(kr) = 2J_1(kr)/(kr) - J_0(kr)$],

$$\int_{k_1}^{k_N} dkkh(k)J_0(rk) = \frac{1}{r}[k_N h_N J_1(rk_N) - k_1 h_1 J_1(rk_1)] - \frac{1}{\delta r^3}\sum_{j=1}^{N-1}(h_{j+1}-h_j)[S_0(rk_{j+1}) - S_0(rk_j)],$$

$$\int_{k_1}^{k_N} dkh(k)J_1(rk) = -\frac{1}{r}[h_N J_0(rk_N) - h_1 J_0(rk_1)] + \frac{1}{\delta r^2}\sum_{j=1}^{N-1}(h_{j+1}-h_j)[R_0(rk_{j+1}) - R_0(rk_j)], \tag{C1}$$

$$\int_{k_1}^{k_N} dkkh(k)J_2(rk) = -\frac{1}{r^2}\{h_N[2J_0(rk_N) + rk_N J_1(rk_N)] - h_1[2J_0(rk_1) + rk_1 J_1(rk_1)]\} + \frac{1}{\delta r^3}\sum_{j=1}^{N-1}(h_{j+1}-h_j)[Q_0(rk_{j+1}) - Q_0(rk_j)],$$

where the functions H_n are the Struve functions (see the next section) and where

$$S_0(x) \equiv \int_0^x dyyJ_1(y) = \frac{\pi}{2}x[J_1(x)H_0(x) - J_0(x)H_1(x)],$$

$$R_0(x) \equiv \int_0^x dyJ_0(y) = xJ_0(x) + S_0(x), \tag{C2}$$

$$Q_0(x) \equiv 3S_0(x) + 2xJ_0(x).$$

In the evaluations of these integrals we used the approximations for the Struve functions H_0 and H_1 of the following section.

2. Approximation of the Struve function $H_0(x)$

As underlined by Aarts and Janssen in a recent paper,[35] the Struve functions are not available in most usual software (for example, MATLAB that is used in the present investigation) and the expansions or approximations available need separate expressions for small or large argument. The authors of Ref. 35 develop an effective and simple approximation for $H_1(z)$ valid for all z, that is,

$$H_1(x) \simeq \frac{2}{\pi} - J_0(x) + \left(\frac{16}{\pi} - 5\right)\frac{\sin x}{x} + 12\left(1 - \frac{3}{\pi}\right)\frac{1-\cos x}{x^2}, \tag{C3}$$

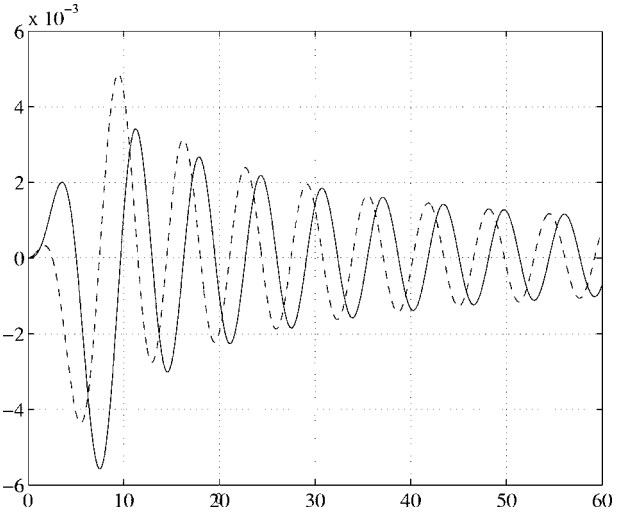

FIG. 16. Full line: absolute error in the approximation of $H_0(x)$ given by Eq. (C8). Dotted line: absolute error in the approximation of $H_1(x)$ given in Ref. 35.

with a maximum absolute error of 0.005 (see also Ref. 36). In the same manner, it is possible to derive an equivalent for the Struve function $H_0(x)$. The function $H_0(x)$ is defined by

$$H_0(x) \equiv \frac{2}{\pi}\int_0^1 dt\frac{\sin xt}{\sqrt{1-t^2}}, \tag{C4}$$

and we use the definition of the Bessel function,

$$J_1(x) \equiv \frac{2x}{\pi}\int_0^1 dt\sqrt{1-t^2}\cos xt. \tag{C5}$$

The preceding integral is integrated by parts, with $f=\sqrt{1-t^2}$ and $g'=\cos xt$. We get

$$J_1(x) = \frac{2}{\pi}\int_0^1 dt\frac{t\sin xt}{\sqrt{1-t^2}}. \tag{C6}$$

The identity $t/\sqrt{1-t^2} = -1/\sqrt{1-t^2} + \sqrt{(1-t)/(1+t)}$ gives

$$J_1(x) = \frac{2}{\pi}\int_0^1 dt\frac{\sin xt}{\sqrt{1-t^2}} + \frac{2}{\pi}\int_0^1 dt\sqrt{\frac{1-t}{1+t}}\sin xt. \tag{C7}$$

We use now the result of Aarts and Janssen:[35] on the interval $[0, 1]$, the function $\sqrt{(1-t)/(1+t)}$ can be approximated by a linear function $\hat{c}+\hat{d}t$, with $\hat{c}=7\pi/2-10$ and $\hat{d}=18-6\pi$ are the values of $\mathcal{C}$ and $\mathcal{D}$ that minimize $\int_0^1 dt|\sqrt{(1-t)/(1+t)} - (\mathcal{C}+\mathcal{D}t)|^2$, from which we get the equivalent for $H_0(x)$,

$$H_0(x) \simeq J_1(x) + \left(\frac{16}{\pi} - 5\right)\frac{1-\cos x}{x} + 12\left(\frac{3}{\pi} - 1\right)\frac{\sin x - x}{x^2}. \tag{C8}$$

The absolute approximation error in Eq. (C8) is plotted in Fig. 16. For the calculation of $H_0(x)$, the computer program MATLAB has been used (the program is a direct conversion of the corresponding FORTRAN program in Ref. 37 by Barrowes[38]). The program uses the power series expansion[39]

$$H_0(x) = \frac{2}{\pi}\left[x - \frac{x^3}{3^2} + \frac{x^5}{3^2 5^2} - \cdots\right]. \tag{C9}$$

As for the H_1 approximation of Aarts and Janssen, the error is small (the maximum value is 0.0056) and vanishes for large x.

[1] X. Xu, S. P. Beckman, P. Specht, E. R. Weber, D. C. Chrzan, R. P. Erni, I. Arslan, N. Browning, A. Bleloch, and C. Kisielowski, Phys. Rev. Lett. **95**, 145501 (2005); K. Arakawa, M. Hatanaka, E. Kuramoto, K. Ono, and H. Mori, *ibid.* **96**, 125506 (2006).

[2] A. V. Granato and K. Lücke, in *Physical Acoustics*, edited by W. P. Mason (Academic, New York, 1966), Vol. 4A.

[3] H. Ogi, N. Nakamura, M. Hirao, and H. Ledbetter, Ultrasonics **42**, 183 (2004); H. Ogi, H. Ledbetter, S. Kim, and M. Hirao, J. Acoust. Soc. Am. **106**, 660 (1999); H. Ledbetter and C. Fortunko, J. Mater. Res. **10**, 1352 (1995).

[4] A. C. Anderson, in *Dislocations in Solids*, edited by F. R. N. Nabarro (North-Holland, New York, 1983), Chap. 29.

[5] A. Maurel, J.-F. Mercier, and F. Lund, Phys. Rev. B **70**, 024303 (2004).

[6] A. Maurel, J.-F. Mercier, and F. Lund, J. Acoust. Soc. Am. **115**, 2773 (2004).

[7] A. Maurel, V. Pagneux, F. Barra, and F. Lund, Phys. Rev. B **72**, 174110 (2005).

[8] A. Maurel, V. Pagneux, F. Barra, and F. Lund, Phys. Rev. B **72**, 174111 (2005).

[9] A. Maurel, V. Pagneux, D. Boyer, and F. Lund, Mater. Sci. Eng., A **400**, 222 (2005).

[10] A. Maurel, V. Pagneux, D. Boyer, and F. Lund, Proc. R. Soc. London, Ser. A **462**, 2607 (2006).

[11] E. Zolotoyabko, D. Shilo, and E. Lakin, Mater. Sci. Eng., A **309**, 23 (2001).

[12] D. Shilo and E. Zolotoyabko, Ultrasonics **40**, 921 (2002).

[13] D. Shilo and E. Zolotoyabko, Phys. Rev. Lett. **91**, 115506 (2003).

[14] D. H. Hurley, O. B. Wright, O. Matsuda, T. Suzuki, S. Tamura, and Y. Sugawara, Phys. Rev. B **73**, 125403 (2006).

[15] C. L. Pekeris, Geophysics **41**, 469 (1955).

[16] K. M. Case and R. D. Hazeltine, J. Math. Phys. **11**, 2546 (1970).

[17] L. R. Johnson, Geophys. J. R. Astron. Soc. **37**, 99 (1974).

[18] T. J. Royston, Y. Yazicioglu, and F. Loth, J. Acoust. Soc. Am. **113**, 1109 (1999).

[19] J. D. Achenbach, J. Acoust. Soc. Am. **106**, 83 (1999).

[20] J. D. Achenbach, Int. J. Solids Struct. **37**, 7043 (2000).

[21] J. D. Achenbach, J. Acoust. Soc. Am. **107**, 1892 (2000).

[22] L. D. Landau and E. M. Lifshitz, in *Theory of Elasticity* (Pergamon, Oxford, 1986).

[23] R. Barakat and B. H. Parshall, Appl. Math. Lett. **9**, 21 (1996).

[24] R. Barakat and B. H. Parshall, Appl. Math. Lett. **11**, 127 (1998).

[25] R. Barakat and B. H. Parshall, Comput. Math. Appl. **40**, 1037 (2000).

[26] T. Suzuki, M. Aoki, and A. Ikushima, Acta Metall. **12**, 1231 (1964).

[27] W. P. Mason and A. Rosenberg, Phys. Rev. **151**, 434 (1966).

[28] T. Ninomiya, J. Phys. Soc. Jpn. **36**, 399 (1974).

[29] F. Lund, J. Mater. Res. **3**, 280 (1988).

[30] T. Mura, Philos. Mag. **8**, 843 (1963).

[31] F. R. N. Nabarro, *Theory of Crystal Dislocations* (Oxford University Press, New York, 1967).

[32] H. Kleinert, *Gauge Fields in Condensed Matter, Part III: Gauge Fields in Solids* (World Scientific, Singapore, 1990).

[33] A. Iserles, IMA J. Numer. Anal. **24**, 365 (2004).

[34] A. Iserles and S. P. Norsett, Math. Comput. **75**, 1233 (2006).

[35] R. M. Aarts and A. J. E. M. Janssen, J. Acoust. Soc. Am. **113**, 2635 (2003).

[36] http://mathworld.wolfram.com/StruveFunction.html

[37] S. Zhang and J. Jin, *Computation of Special Functions* (Wiley, New York, 1996).

[38] Ben Borrowes, http://ceta.mit.edu/comp_spec_func/

[39] M. Abramowitz and I. A. Stegun, *Handbook of Mathematical Functions with Formulas, Graphs, and Mathematical Tables* (Dover, New York, 1964), p. 12.1.4.